Supplementary Materials for

Exploiting hidden singularity on the surface of the Poincaré sphere

Jinxing Li[1,†], Aloke Jana[2,†], Yueyi Yuan[1], Kuang Zhang[1]*, Shah Nawaz Burokur[3*], and Patrice Genevet[2]*

Affiliations:

[1] Department of Microwave Engineering, Harbin Institute of Technology, Harbin, 150001, China

[2] Department of Physics, Colorado School of Mines, 1523 Illinois, St, Golden, CO 80401, USA

[3] LEME, Univ Paris Nanterre, 92410 Ville d'Avray, France

*Corresponding author. zhangkuang@hit.edu.cn, sburokur@parisnanterre.fr, patrice.genevet@mines.edu

†These authors contributed equally to this work.

The PDF file includes:

Supplementary Text

Supplementary Note 1: Evolution of Polarization state, Berry curvature and associated geometric phase

For a lossless Hermitian paraxial optical device with eigenstates $|n_{\pm}\rangle$ and corresponding eigenvalues $e^{i\phi_{\pm}}$, the polarization-dependent transmission response can be characterized by the governing unitary operator $\widehat{U}$, represented by the Jones matrix of the system. The orthonormal polarization bases of the ket vector are considered as right- and left-handed circular polarization (RHCP and LHCP), denoted as $|R\rangle$ and $|L\rangle$, respectively. The Stokes parameters corresponding to the direction vector $\hat{\boldsymbol{n}}$ pointing at $(2\psi,2\chi)$ define the eigenstate of the system (Fig. S1), where ψ represents the azimuthal angle and χ corresponds to the ellipticity. The eigenstate $|n_{+}\rangle$ is given by:

$$|n_{+}\rangle = \begin{pmatrix} S_1 \\ S_2 \\ S_3 \end{pmatrix} = \begin{pmatrix} \cos 2\chi \cos 2\psi \\ \cos 2\chi \sin 2\psi \\ \sin 2\chi \end{pmatrix} \tag{S1}$$

The system's orthonormal eigenvectors $|n_{\pm}\rangle$ can be expressed in terms of circular polarization basis as follows:

$$|n_{+}\rangle = \cos\left(\frac{\pi}{4}-\chi\right)e^{i\psi}|R\rangle + \sin\left(\frac{\pi}{4}-\chi\right)e^{-i\psi}|L\rangle = \begin{pmatrix} \cos\left(\frac{\pi}{4}-\chi\right)e^{i\psi} \\ \sin\left(\frac{\pi}{4}-\chi\right)e^{-i\psi} \end{pmatrix} \tag{S2a}$$

$$|n_{-}\rangle = -\sin\left(\frac{\pi}{4}-\chi\right)e^{i\psi}|R\rangle + \cos\left(\frac{\pi}{4}-\chi\right)e^{-i\psi}|L\rangle = \begin{pmatrix} -\sin\left(\frac{\pi}{4}-\chi\right)e^{i\psi} \\ \cos\left(\frac{\pi}{4}-\chi\right)e^{-i\psi} \end{pmatrix} \tag{S2b}$$

Notably, the eigenvector $|n_{-}\rangle$ is at the antipodal point of $|n_{+}\rangle$ on the Poincaré sphere, having an azimuth and ellipticity of $\psi + \pi/2$ and $-\chi$, respectively.

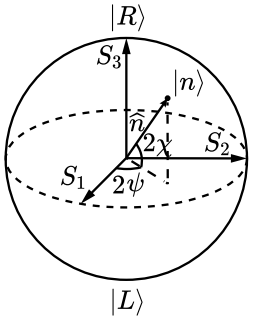

Poincaré sphere

Fig. S1. Geometrical representation of a polarization state on the Poincaré sphere. The north and south poles of the Poincaré sphere is $|R\rangle$ and $|L\rangle$, and the angular coordinate is $(2\psi,2\chi)$, where ψ and χ represent the azimuth angle and ellipticity of the polarization state, respectively.

Any given polarization state can be represented by the intensity normalized Cartesian coordinates of the Stokes vector (S_1, S_2, S_3). The north and south poles of the conventional Poincaré sphere represent the right- and left-handed circular polarization states, respectively, denoted as $|R\rangle$ and $|L\rangle$ while the equator corresponds to linearly polarized states. An arbitrary eigen polarization state $|n_+\rangle$ on the surface of the Poincaré sphere is described by angular coordinates 2ψ and 2χ, where ψ represents the azimuth angle and χ denotes the ellipticity of the polarization state.

In the circular polarization basis, the unitary operator governing a lossless Hermitian optical system, represented by its Jones matrix, can be expressed in terms of the Pauli spin matrices as:

$$\widehat{U} = |n_+\rangle\langle n_+|e^{i\phi_+} + |n_-\rangle\langle n_-|e^{i\phi_-} = \exp\left(i\frac{\delta}{2}\hat{n}\cdot\widehat{\boldsymbol{\sigma}}^* + i\phi\right)$$
$$= e^{i\phi}\begin{pmatrix} \cos\frac{\delta}{2} + i\sin\frac{\delta}{2}\sin 2\chi & i\sin\frac{\delta}{2}\cos 2\chi\, e^{i2\psi} \\ i\sin\frac{\delta}{2}\cos 2\chi\, e^{-i2\psi} & \cos\frac{\delta}{2} - i\cos\frac{\delta}{2}\sin 2\chi \end{pmatrix} = \begin{pmatrix} t_{++} & t_{+-} \\ t_{-+} & t_{--} \end{pmatrix} \quad \text{(S3)}$$

where the dynamical phase $\phi = \frac{\phi_+ + \phi_-}{2}$ and the retardance (birefringence of the system) $\delta = \phi_+ - \phi_-$, are the mean and difference eigenvalues' phase ϕ_+ and ϕ_-, and $\widehat{\boldsymbol{\sigma}} = \left(\hat{\sigma}_x, \hat{\sigma}_y, \hat{\sigma}_z\right)$ is the vector of Pauli spin matrices consisting of three basic spin matrices. Please note that the application of sigma conjugation ensures a positive azimuthal rotation (anti-clockwise) of linear/elliptical polarization states, which is consistence with the phase factors considered in circular basis states in Eq. S2(a-b).

$$\hat{\sigma}_x = \begin{pmatrix} 0 & 1 \\ 1 & 0 \end{pmatrix}, \hat{\sigma}_y = \begin{pmatrix} 0 & -i \\ i & 0 \end{pmatrix}, \hat{\sigma}_z = \begin{pmatrix} 1 & 0 \\ 0 & -1 \end{pmatrix} \quad \text{(S4)}$$

When a normal incident wave of polarization $|\Psi_0\rangle$ interacts with an eigen system described by Eq. S3, the resulting output state is given by $|\Psi\rangle = \widehat{U}|\Psi_0\rangle$. The co-polarized transmittance (t_{co}), is defined as the inner product of the input and output polarization states:

$$t_{co} = |t_{co}|e^{i\zeta} = \langle\Psi_0|\widehat{U}|\Psi_0\rangle \quad \text{(S5)}$$

Let us assume the RHCP wave as input, i.e. $|\Psi_0\rangle = |R\rangle$. In this case, the complex transmittance in the co-polarized channel is $t_{co} = \cos\frac{\delta}{2} + i\sin\frac{\delta}{2}\sin 2\chi$, indicating that t_{co} is governed by the eigen birefringence δ and eigen ellipticity χ. Herein, the coordinate in eigen parameter space **R** = (δ, χ) characterizes the property of evolution operator $\widehat{U}$, and thereby controlling the dynamics of complex transmission amplitude in co-polarized channels. Following a path in eigen parameter space, the accumulated phase along the path corresponds to a set of meta-atoms, which can be designed to engineer the phase response of the co-polarized wave. Therefore, it is necessary to characterize the phase difference between any points along the path. In other words, a connection needs to be constructed to compare the phase between arbitrary two points along the path. As the two points **R** and **R** + d**R** in the parameter space are closely adjacent (d**R** → 0), the phase difference ($\Delta\zeta(\mathbf{R})$) is

$$e^{i\Delta\zeta(\mathbf{R})} = \frac{e^{i\zeta(\mathbf{R}+\mathrm{d}\mathbf{R})}}{e^{i\zeta(\mathbf{R})}} = \frac{\langle\Psi_0|\widehat{U}(\mathbf{R}+\mathrm{d}\mathbf{R})|\Psi_0\rangle}{\langle\Psi_0|\widehat{U}(\mathbf{R})|\Psi_0\rangle} \times \frac{|\langle\Psi_0|\widehat{U}(\mathbf{R})|\Psi_0\rangle|}{|\langle\Psi_0|\widehat{U}(\mathbf{R}+\mathrm{d}\mathbf{R})|\Psi_0\rangle|} \tag{S6}$$

According to equivalent infinitesimal, there is

$$\frac{|\langle\Psi_0|\widehat{U}(\mathbf{R})|\Psi_0\rangle|}{|\langle\Psi_0|\widehat{U}(\mathbf{R}+\mathrm{d}\mathbf{R})|\Psi_0\rangle|} \to 1, e^{ix} \to 1 + ix \tag{S7}$$

Eq. S7 turns to

$$e^{i\Delta\zeta(\mathbf{R})} \approx \frac{\langle\Psi_0|\widehat{U}(\mathbf{R}+\mathrm{d}\mathbf{R})|\Psi_0\rangle}{\langle\Psi_0|\widehat{U}(\mathbf{R})|\Psi_0\rangle} \to 1 + i\Delta\zeta(\mathbf{R}) \tag{S8}$$

The middle term in Eq. S8 can be expanded according to the Taylor series

$$\frac{\langle\Psi_0|\widehat{U}(\mathbf{R}+\mathrm{d}\mathbf{R})|\Psi_0\rangle}{\langle\Psi_0|\widehat{U}(\mathbf{R})|\Psi_0\rangle} = \frac{t_{co}(\mathbf{R}+\mathrm{d}\mathbf{R})}{t_{co}(\mathbf{R})} \to 1 + \frac{\frac{\partial t_{co}(\mathbf{R})}{\partial\mathbf{R}} \cdot \mathrm{d}\mathbf{R}}{t_{co}(\mathbf{R})} + \cdots \tag{S9}$$

Combining Eq. S8 and S9, $\Delta\zeta(\mathbf{R})$ can be derived as

$$\Delta\zeta(\mathbf{R}) = -i\frac{\left\langle\Psi_0\left|\frac{\partial\widehat{U}(\mathbf{R})}{\partial\mathbf{R}}\right|\Psi_0\right\rangle}{\langle\Psi_0|\widehat{U}(\mathbf{R})|\Psi_0\rangle} \cdot \mathrm{d}\mathbf{R} = Im\left(\frac{\boldsymbol{\partial}}{\boldsymbol{\partial R}}\ln\langle\Psi_0|\widehat{U}(\mathbf{R})|\Psi_0\rangle\right) \cdot \mathrm{d}\mathbf{R} \tag{S10}$$

The phase difference between any two points along the path can be expressed as the path integral of the Berry connection term $\boldsymbol{\mathcal{A}_0}(\mathbf{R}) = i\frac{\boldsymbol{\partial}}{\boldsymbol{\partial R}}\ln\langle\Psi_0|\widehat{U}(\mathbf{R})|\Psi_0\rangle$. Accordingly, the associated geometric Berry phase in the parameter space is defined as:

$$\phi_G(\boldsymbol{R}) = \int_{\mathbf{R}_1}^{\mathbf{R}_2} \boldsymbol{\mathcal{A}_0}(\mathbf{R}) \cdot \mathrm{d}\mathbf{R} \tag{S11}$$

The accumulated geometric phase $\phi_G = -\zeta(\mathbf{R})$ (with the negative sign convention) depends on the curvature of the path taken from $\boldsymbol{R}_1$ to $\boldsymbol{R}_2$ in the eigen parameter space **R**, which characterizes the instantaneous eigen states of the system. This formulation closely resembles the classical geometric Berry phase, where phase accumulation is derived from the instantaneous evolution of eigenstates in configuration space. However, a subtle difference in this approach is that instead of analyzing the evolution of the system's eigenstates directly, we track down the evolution of an input polarization governed by the unitary operator, expressed as $|\Psi\rangle = \widehat{U}(\mathbf{R})|\Psi_0\rangle$. And $|\Psi\rangle$ is subsequently projected onto the same initial input state $|\Psi_0\rangle$ using the projection operator $\hat{P} = |\Psi_0\rangle\langle\Psi_0|$ on the Poincare sphere. Therefore, the accumulation of geometric phase in the co-polarization transmission channel depends on the eigen parameters **R**

= (δ, χ), which can also be mapped at the Stokes parametric position of $|\Psi\rangle$ on the surface of the Poincare sphere, as illustrated in the next section.

Supplementary Note 2: Manifestation of hidden singularity on the surface of the Poincaré sphere

Let us denote the output state $|\Psi(\mathbf{R}_s)\rangle = \widehat{U}(\mathbf{R})|\Psi_0\rangle$, where $\mathbf{R}_s$ represents the angular coordinates of $|\Psi\rangle$ on the Poincaré sphere. Eq. S5 has shown that the co-polarized transmittance t_{co} only depends on eigen parameters: birefringence δ and ellipticity χ and is free from azimuth ψ. In other words, $|\Psi_0\rangle$ is acted by the operator after eliminating the influence of azimuth ψ (azimuth ψ can be regarded as a constant), and $|\Psi(\mathbf{R}_s)\rangle$ is the partial evolution state of the actual evolution state after removing the effect of azimuth angle. For simplicity, when ψ is fixed at $-\pi/2$ to set t_{-+} a real number, the output state $|\Psi(\mathbf{R}_s)\rangle$ can be mapped on the Poincaré sphere according to:

$$|\Psi(\mathbf{R}_s)\rangle = \begin{pmatrix} t_{co} \\ \sqrt{1-|t_{co}|^2} \end{pmatrix} = \begin{pmatrix} \cos\frac{\delta}{2} + i\sin\frac{\delta}{2}\sin 2\chi \\ \sin\frac{\delta}{2}\cos 2\chi \end{pmatrix} = \begin{pmatrix} \cos\left(\frac{\pi}{4}-\chi_s\right)e^{i2\psi_s} \\ \sin\left(\frac{\pi}{4}-\chi_s\right) \end{pmatrix} \tag{S12}$$

The azimuth angle $2\psi_s$ and elevation angle $2\chi_s$ on the Poincaré sphere are:

$$2\chi_s = 2\left(\frac{\pi}{4} - \operatorname{atan}\frac{\sqrt{1-|t_{co}|^2}}{|t_{co}|}\right) \tag{S13a}$$

$$2\psi_s = \arg(t_{co}) \tag{S13b}$$

where arg() denotes the argument function. The mapping between $(2\chi_s, 2\psi_s)$ and (δ, χ) is depicted in Fig. S2A and B, where the angular coordinate in the parameter space can completely cover Poincaré sphere. So far, the complete mapping between $(2\chi_s, 2\psi_s)$ and (δ, χ) is established. Next, the transmission amplitude and phase at each (δ, χ) in parameter space are mapped onto the Poincaré sphere according to the mapping between $(2\chi_s, 2\psi_s)$ and (δ, χ) in Fig. S2A and B.

Fig. S2C clearly shows that the singularity of amplitude in the parameter space is exactly at the south pole of Poincaré sphere, the polarization state $|L\rangle$, which is the antipole of the RHCP incident wave. The phase around the singularity changes by 2π continuously along the parallel but constant along the meridian. Consequently, the phase difference between any two closely adjacent points ($\mathrm{d}\mathbf{R}_s \to 0$) on the sphere is

$$e^{i\Delta\zeta(\mathbf{R}_s)} = \frac{\langle\Psi_0|\Psi(\mathbf{R}_s + \mathrm{d}\mathbf{R}_s)\rangle}{\langle\Psi_0|\Psi(\mathbf{R}_s)\rangle} \to 1 + i\Delta\zeta(\mathbf{R}_s) \tag{S14a}$$

$$\Delta\zeta(\mathbf{R}_s) = -i\frac{\left\langle\Psi_0\left|\frac{\partial}{\partial\mathbf{R}_s}\right|\Psi(\mathbf{R}_s)\right\rangle}{\langle\Psi_0|\Psi(\mathbf{R}_s)\rangle}\cdot\mathrm{d}\mathbf{R}_s = \mathrm{Im}\frac{\left\langle\Psi_0\left|\frac{\partial}{\partial\mathbf{R}_s}\right|\Psi(\mathbf{R}_s)\right\rangle}{\langle\Psi_0|\Psi(\mathbf{R}_s)\rangle}\cdot\mathrm{d}\mathbf{R}_s \tag{S14b}$$

According to the phase distribution in Fig. S2D, the derivative of phase on the sphere is

$$\mathrm{Im}\frac{\left\langle \Psi_0 \middle| \frac{\partial}{\partial \mathbf{R}_s} \middle| \Psi(\mathbf{R}_s) \right\rangle}{\langle \Psi_0 | \Psi(\mathbf{R}_s) \rangle} = \frac{1}{\cos 2\chi} \hat{e}_{2\psi} \tag{S15a}$$

$$\mathrm{d}\mathbf{R}_s = \cos 2\chi \, d2\psi(\mathbf{R}_s)\hat{e}_{2\psi} + d2\chi(\mathbf{R}_s)\hat{e}_{2\chi} \tag{S15b}$$

where $\hat{e}_{2\psi}$ and $\hat{e}_{2\chi}$ are the orthogonal unit vectors along azimuthal and elevation direction, $2\psi(\mathbf{R}_s)$ and $2\chi(\mathbf{R}_s)$ are the azimuthal and elevation angles of point $\mathbf{R}_s$.

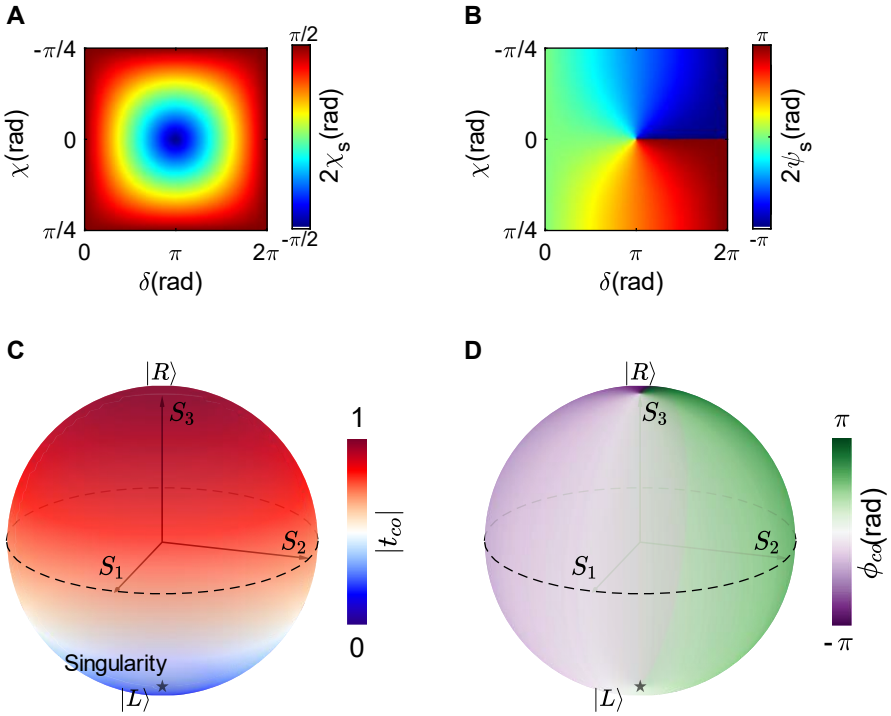

Fig. S2. Map complex amplitude t_{co} from parameter space to Poincaré sphere. (**A**) The elevation angle $2\chi_s$ and (**B**) azimuth angle $2\psi_s$ in the eigen parameter space of (δ, χ). (**C**) The amplitude and (**D**) phase of t_{co} mapped onto Poincaré sphere, the singularity (star mark) is on the south pole and the maximum amplitude is on the north pole, the singularity is always at the antipole of the maximum amplitude. The phase around the singularity shifts by 2π along parallel continuously and remains unchanged along the meridian.

Consequently, by substituting Eq. S15 into Eq. S14b and then integrate $\Delta\zeta(\mathbf{R}_s)$ along a path starting from an initial point $\mathbf{R}_0$ to target point $\mathbf{R}_s$ the integration can be simplified as

$$\zeta(\mathbf{R}_s) = \int_{\mathbf{R}_0}^{\mathbf{R}_s} \Delta\zeta(\mathbf{R}_s) \cdot \mathrm{d}\mathbf{R} = \int_{\mathbf{R}_0}^{\mathbf{R}_s} 1\mathrm{d}2\psi(\mathbf{R}_s) = 2\psi(\mathbf{R}_s) - 2\psi(\mathbf{R}_0) \tag{S16}$$

Eq. S16 shows that the integration only depends on the azimuthal angle of the starting and ending points, which is purely geometric. To demonstrate the geometric property of the phase accumulation, we calculate the phase accumulation along three different smooth closed loops outside (solid circle), crossing (dashed circle) and encircling (dotted circle) the singularity, which are similar to the curves in Fig. 2 in the main text (Fig. S3A and B). For the sake of clarity, here

we denote the angle of the circle on parameter space as α, and the paths on Poincaré sphere are projected to the equatorial plane (Fig. S3C) because the phase accumulation along the paths on the sphere only depends on the azimuthal angle.

The phase accumulation result in Fig. S3D is directly calculated by Eq. S5 and acts as a reference. Figs. S3E and F show the phase results calculated by the integration of Eqs. S14b and 16, respectively. Obviously, the phase curves in Fig. S3E and F are the same as the reference results in Fig. S3D, where the phase accumulation range of the solid, dashed and dotted curves is less than π, equal to π and 2π, respectively. The results validate Eq. S11 and Eq. S16 and demonstrate that encircling the singularity can gain 2π phase accumulation, indicating the topologically protected property of the co-polarized singular phase.

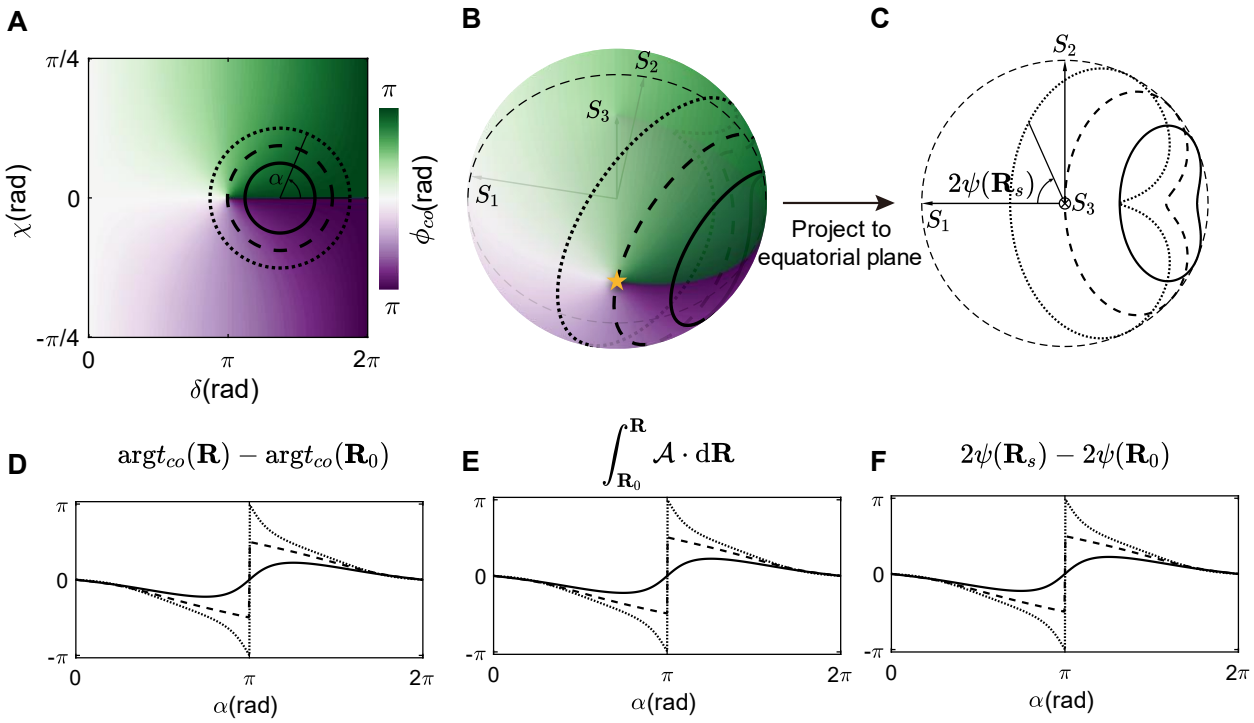

Fig. S3. Phase accumulation along loops outside, crossing and encircling the singularity. Three different smooth closed loops outside (solid circle), crossing (dashed circle) and encircling (dotted circle) the singularity in (**A**) parameter space and (**B**) Poincaré sphere. (**C**) The projected paths on the equatorial plane. The phase accumulation along the three paths calculated by (**D**) Eq. S5, (**E**) Eq. S11 and (**F**) Eq. S16.

Supplementary Note 3: Co-polarized singular phase and associated topology protection

To understand the behaviour of the co-polarized singular phase and its associated topology protection, we first plot the co-polarized phase in the eigen parameter space **R** = (δ, χ) as we have discussed in the main text (Fig. S4A) in great details. This phase is then mapped onto a toroidal surface T^2 to capture its periodicity and topological properties. In Fig. S4B, the toroidal surface T^2 is visualized by considering δ as the azimuthal angle and ϕ_{co} as the poloidal angle of the torus surface, respectively. The dashed loop represents a closed trajectory in the eigen parameter space that does not enclose the singularity, leading to a total phase accumulation along the loop is zero. Since the loop can be smoothly deformed out of the torus, it corresponds to a trivial topology with a Chern number of $C = 0$, indicating no topological protection.

In contrast, the solid loop encloses the singularity and accumulates a total phase of -2π as it encircles the singular point in an anticlockwise direction. This accumulation is a hallmark of a nontrivial topology, as the loop cannot be smoothly deformed out of the torus without cutting through it. Consequently, it exhibits a topologically protected phase with a Chern number of $C = -1$, ensuring a robust and complete 2π phase accumulation in the co-polarized transmission channel.

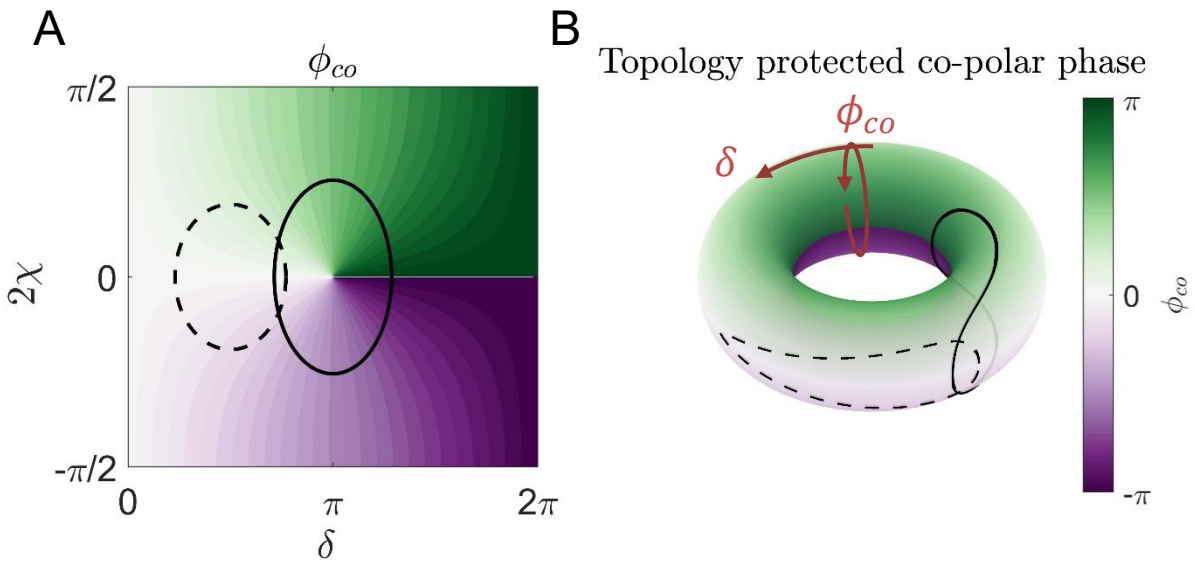

Fig. S4. The enclosing singularity and associated topological protection. (**A**) Two closed loops outside (dashed) and encircling (solid) the co-polarized phase singularity are shown in the eigen parameter space. (**B**) Topological depiction of the co-polarized phase on a toroidal surface. The phase variation along the solid loop is constrained by the toroidal topology, with a Chern number of $C = -1$, leading to a full 2π phase accumulation in the co-polar transmission channel.

Supplementary Note 4: Encircle the singularity of the co-circular channels with maximum efficiency by circular birefringent meta-atom

It has been demonstrated that encircling the singularity enables achieving 2π phase accumulation. It is also necessary to take into account the amplitude along the path since it determines the transmission efficiency. Fig. S5A shows the amplitude on the Poincaré sphere clearly, the larger the elevation angle the higher the amplitude because $|t_{co}| = \cos(\pi/4 - \chi_s)$. For instance, when the evolution loop is extremely close to the north pole, the amplitude on this path is almost unity, but the length of the curve is extremely short (the very tiny green circle near the north pole) making it look like a point and is hardly observable on the sphere. To clearly show the amplitude and phase result simultaneously, the sphere is expanded according to the relationship between the angular coordinate and complex amplitude as follows:

$$\begin{cases} x = |t_{co}| \cos 2\psi_s \\ y = |t_{co}| \sin 2\psi_s \\ z = |t_{co}| = \cos\left(\frac{\pi}{4} - \chi_s\right) \end{cases} \tag{S17}$$

The expanded sphere is shown in Fig. S5B, where the conical surface represents the amplitude and the corresponding phase is projected on the heatmap. The amplitude singularity at the south pole of the sphere turns to the tip of the conical surface, while the phase around the singularity shows a continuous variation of 2π. The extremely short evolution loop on the sphere corresponds to the top edge of the conical surface, which holds a unity amplitude as well as linear 2π phase accumulation, i.e. $t_{++} = \pm e^{i\delta/2}$, and the phase shift is linear to $\delta/2$. According to Eq. S5, there should be $\chi = \pm\frac{\pi}{4}$ and $\delta \in [0,2\pi]$, indicating that the eigenstate of the meta-atom should agree with the incident polarization and the corresponding eigen birefringence needs to be tuned within 0 to 2π.

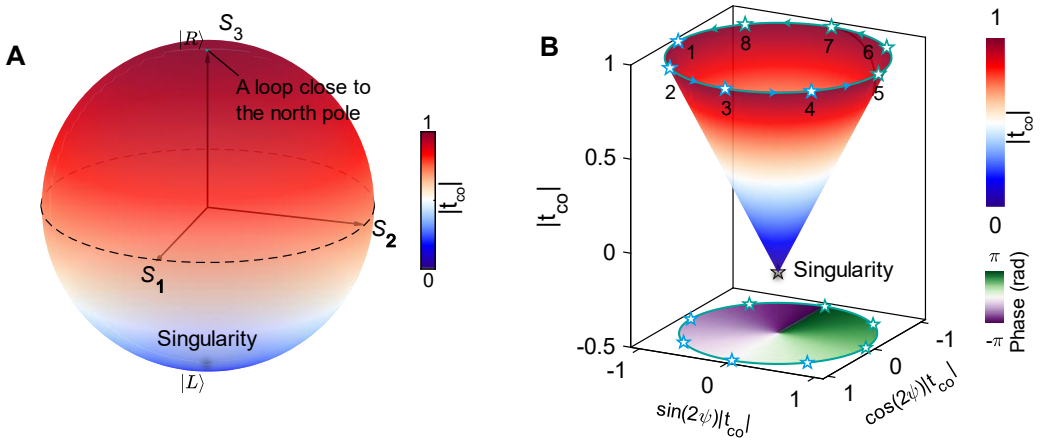

Fig. S5. The enclosing path with amplitude near unity on the Poincaré sphere and the expanded Poincaré sphere. (**A**) The loop path with amplitude approaching unity is extremely close to the north pole, which is shown in an extremely short green loop that is hard to observe. (**B**) Amplitude (conical surface) and phase (bottom heat map) of t_{co} on the expanded Poincaré sphere, the loop path with maximum amplitude is the top edge of the conical surface, and the phase along the path shifts by 2π continuously. The numbered discrete points correspond to the element in Fig. S6B-E.

To encircle the singularity around the top edge of the conical surface under CP incident wave, we design a circular birefringent meta-atom exhibiting high transmission. The detailed schematic structure of the proposed meta-atom is shown in Fig. S6A, which consists of two 2.5 mm thick FB430 dielectric substrates (ε_r = 4.3, tan δ = 0.002), a 0.1 mm thick bonding layer (ε_r = 3.5, tan δ = 0.004), three layers of printed copper pattern and four vertical metal vias. Both the top and bottom copper layers contain four identical patches forming C_{4z} symmetry, which are electrically connected by metal vias to build four patch-via-patch structures that allow direct coupling. Meanwhile, the middle copper layer is a metal ground plane with circular trims (the radius is 0.15 mm larger than the vias) allowing vias to penetrate without any contact with the ground plane. The ground plane allows the patches facing the incidence to directly couple with the incident wave while shielding the patch on another side. As a result, when the EM wave passes through the metasurface, the patch layer facing the incidence acts as a receiver, and the received EM energy is coupled to the patch layer on the other side by the vias, which acts as a transmitter to radiate the energy to free space on the transmission side. Relatively rotating the top and bottom patches connected by the same via can be effectively regarded as changing the polarization angle of the antennas, which causes a circular birefringence δ nearly twice the counterclockwise rotation angle θ ($\delta \approx 2\theta$), and the co-polarized singular phase of the RHCP and LHCP transmitted wave is $\delta/2$ and $-\delta/2$ respectively.

The goal is to engineer the structure to gain 2π accumulation of co-polarized singular phase. For the designed structure, the neighbouring patches may touch each other when the rotation angle θ is over 90°, which will sharply change the property of the meta-atom and deteriorate the performance. To avoid this issue, the bottom patches are fixed and the top patches are rotated counterclockwise around their metal vias within 0°-90°, which is sufficient to tune δ from 0 to π (quarter circle from elements 3 to 5 in Fig. S5) and allows phase modulation of both RHCP and LHCP to realize $\phi_{++} = -\phi_{--} \in [0, \pi/2]$, as shown in Fig. S6C. Subsequently, mirroring the element with respective to the *xoz* plane (or *yoz* plane) effectively inverts the sign of χ while maintaining δ unchanged. Further combined with δ tuning from 0 to π, phase coverage within [-π/2, 0] is achieved (Fig. S6B), thereby extending the total phase range to [-π/2, π/2], complete half-circle loop in the phase diagram in Fig. S5 from elements 1 to 5.

Next, we need to fill the phase range within [π/2, π] and [-π, -π/2] to cover the full phase range. The phase range within [π/2, π] is equal to adding π to the interval [-π/2, 0], hence, denotes the co-polarized singular phase within the two different ranges as $\phi_{++} = -\phi_{--} \in [-\pi/2, 0]$ and $\phi'_{++} = -\phi'_{--} \in [\pi/2, \pi]$, they follow the relationship as below:

$$\phi'_{++} = \phi_{++} + \pi, \phi'_{--} = \phi_{--} - \pi \tag{S18}$$

The corresponding circular birefringence and mean phase are

$$\delta' = \delta + 2\pi, \phi' = \phi = 0 \tag{S19}$$

Substituting them into the operator in Eq. S3, there is

$$\widehat{U}(\delta') = \exp\left(i\frac{\delta + 2\pi}{2}\hat{n} \cdot \hat{\boldsymbol{\sigma}}^*\right) = -\widehat{U}(\delta) \tag{S20}$$

The above equation indicates that there is a polarization independent π-phase difference between the elements with phase covering in the [-π/2, 0] range and those in the [π/2, π] range, which is equivalent to adding a π dynamic phase. Therefore, the distinct geometric size of elements in Fig. S6B and D aims to add a global π-phase difference, and the same applies to elements in Fig. S6C and E. By tuning the elements in Fig. S6D and E in the same way, the phase range within [π/2, π] and [-π, -π/2] is achieved respectively. So far, the engineered elements can completely encircle the singularity to gain 2π accumulation.

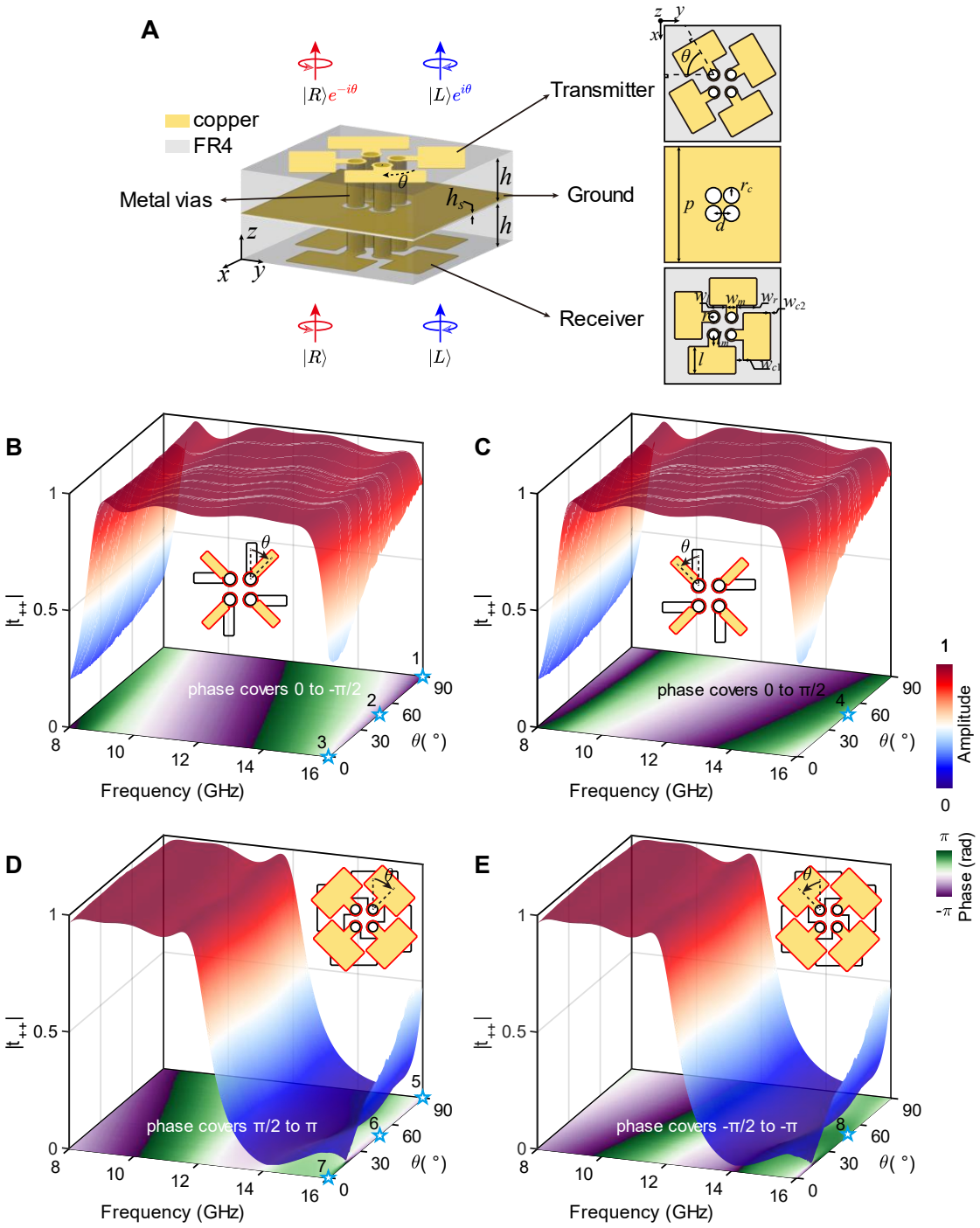

Fig. S6. Tunning circular birefringent meta-atom to completely cover 2π phase accumulation. (**A**) The structure and propagation schematic of meta-atom. The meta-atom consists of four parts: receiver patch, transmitter patch, metal vias, and ground plane. The patches on the receiver and transmitter layer are electrically connected by a via, and the relative rotation angle θ between them can be tuned from 0° to 90°. As the RHCP and LHCP wave pass through the metasurface, the patch layer facing the incidence acts as a receiver antenna, and the received EM energy is coupled to the patch layer on another side by the vias, which acts as a transmitter to radiate the energy to free space on the transmission side. The transmitted RHCP and LHCP gain a $-\theta$ and θ phase respectively (the schematic here is clockwise rotation, while the phase sign is inverted for the case of counterclockwise rotation.). (**B**) The complex transmittance of meta-atom (inset shows its shape) covering the phase shift will decrease from 0 to -π/2 as the relative rotation angle θ increases from 0° to 90° clockwise, covering phase range of [-π/2,0] and obtaining elements 1 to 3. Mirror the structure with respective to *xoz* plane and increase θ from 0 to π/2 counterclockwise, (**C**) the amplitude is almost unchanged while the corresponding phase coverage becomes [0,π/2], and element 4 is realized. (**D**) By increasing the patch size to introduce a polarization-independent π phase shift to elements 1 to 3, the spectrum undergoes a redshift and results in a corresponding phase range of [π/2, π] to obtain elements 5 to 7. (**E**) In the same way, mirror the structure in D to cover phase shift within [-π,-π/2] and obtain element 8.

Note that the transmission amplitude in Fig. S6B to E cannot perfectly reach unity, which is due to reflection rather than loss. The total reflection amplitude results corresponding to the transmission in Fig. S6B and D are shown in Fig. S7A and B. It is evident that the decrease of the transmission exactly corresponds to the increase of reflection, proving that the meta-atom is almost lossless and reflection reduces the structure's overall transmission. Furthermore, the medium property of the designed meta-atom is analyzed by generalized sheet transition conditions (GSTCs) theory (*28*) to illustrate its working mechanism.

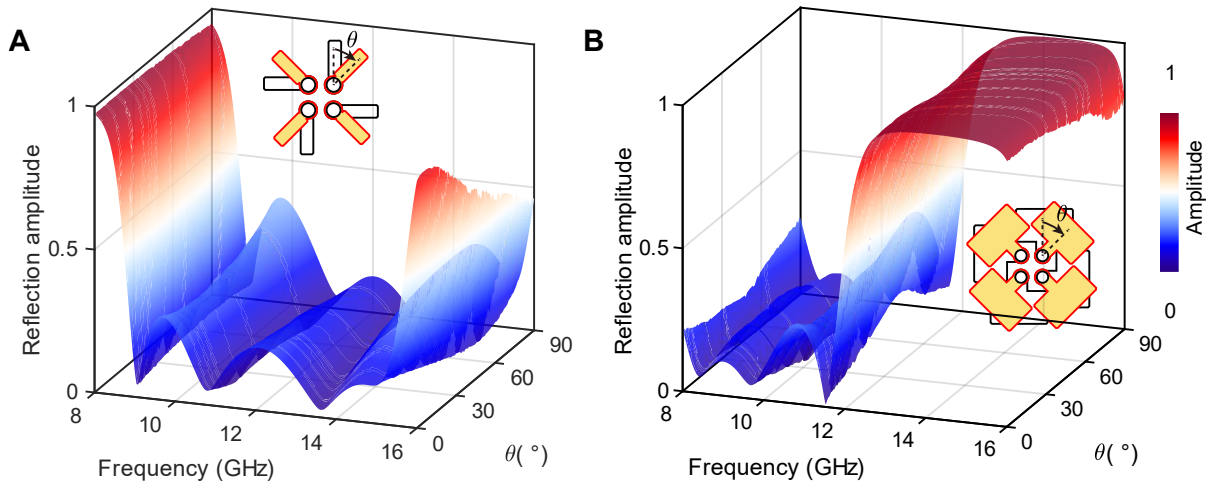

Fig. S7. Reflection amplitude of the circular birefringent meta-atoms. (A) The reflection amplitude of (**A**) the meta-atom in Fig.S6B and (**B**) Fig.S6D as the relative rotation angle θ is increased from 0 to π/2 clockwise.

According to GSTCs theory, when normal incident waves illuminate a two-dimensional (2D) uniform metasurface, the equivalent surface electric current and magnetic current ($\mathbf{J}^s$ and $\mathbf{M}^s$) can

be induced on the metasurface. The relationship between the excitation field and the constitutive property of the meta-atom is described as:

$$\begin{pmatrix} \mathbf{J}^s \\ \mathbf{M}^s \end{pmatrix} = \begin{pmatrix} \boldsymbol{\chi}_{ee} & \boldsymbol{\chi}_{em} \\ \boldsymbol{\chi}_{me} & \boldsymbol{\chi}_{mm} \end{pmatrix} \begin{pmatrix} \mathbf{E}^{av} \\ \mathbf{H}^{av} \end{pmatrix} \tag{S21}$$

where $\mathbf{J}^s = [J_x^s \quad J_y^s]^{\mathrm{T}}$ and $\mathbf{M}^s = [M_x^s \quad M_y^s]^{\mathrm{T}}$, and $\mathbf{E}^{av} = [E_x^{av} \quad E_y^{av}]^{\mathrm{T}}$, $\mathbf{H}^{av} = [H_x^{av} \quad H_y^{av}]^{\mathrm{T}}$ are the average tangential electric and magnetic vector fields to surface, and superscript T denotes transpose. The $\boldsymbol{\chi}_{ee}$, $\boldsymbol{\chi}_{mm}$, $\boldsymbol{\chi}_{em}$, $\boldsymbol{\chi}_{me}$ are all the 2 × 2 tensors of electric, magnetic, magnetic-to-electric and electric-to-magnetic equivalent susceptibility, presenting the following form:

$$\begin{aligned} \boldsymbol{\chi}_{ee} &= \begin{pmatrix} \chi_{ee}^{xx} & \chi_{ee}^{xy} \\ \chi_{ee}^{yx} & \chi_{ee}^{yy} \end{pmatrix}, \quad \boldsymbol{\chi}_{em} = \begin{pmatrix} \chi_{em}^{xx} & \chi_{em}^{xy} \\ \chi_{em}^{yx} & \chi_{em}^{yy} \end{pmatrix} \\ \boldsymbol{\chi}_{me} &= \begin{pmatrix} \chi_{me}^{xx} & \chi_{me}^{xy} \\ \chi_{me}^{yx} & \chi_{me}^{yy} \end{pmatrix}, \quad \boldsymbol{\chi}_{mm} = \begin{pmatrix} \chi_{mm}^{xx} & \chi_{mm}^{xy} \\ \chi_{mm}^{yx} & \chi_{mm}^{yy} \end{pmatrix} \end{aligned} \tag{S22}$$

The four tensors totally contain 16 equivalent surface susceptibilities that can characterize the 2D constitutive property of the meta-atom. When the meta-atom is lossless, $\boldsymbol{\chi}_{ee}$ and $\boldsymbol{\chi}_{mm}$ are purely imaginary while $\boldsymbol{\chi}_{em}$ and $\boldsymbol{\chi}_{me}$ are purely real. Therefore, we will focus on the imaginary part of $\boldsymbol{\chi}_{ee}$, $\boldsymbol{\chi}_{mm}$ and the real part of $\boldsymbol{\chi}_{em}$, $\boldsymbol{\chi}_{me}$ because the meta-atom is almost lossless. The 16 susceptibilities can be retrieved from the corresponding scattering parameters (*S* parameters) of the meta-atom:

$$\mathbf{S}_{nm} = \begin{pmatrix} S_{nm}^{xx} & S_{nm}^{xy} \\ S_{nm}^{yx} & S_{nm}^{yy} \end{pmatrix} \tag{S23}$$

where subscripts *n* and *m* = 1, 2, denoting the propagation direction $m \rightarrow n$ (Fig. S8), and the superscripts *xx* and *yx* (*yy* and *xy*) denote co- and cross-polarized responses under *x*- (*y*-) linear polarization (LP) normal incidence respectively.

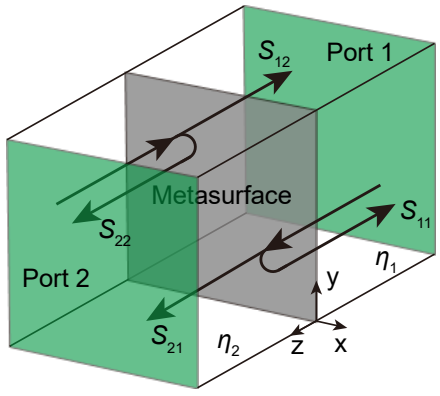

Fig. S8. Normal propagation schematic of the general lossless metasurface. Port 1 and port 2 are located on the two sides of the metasurface. η_1 and η_2 represent the wave impedance of the two regions respectively, and the arrows denote the propagation direction of the wave.

Then, the susceptibilities can be calculated from *S* parameters according to (*29*)

$$\begin{pmatrix} \boldsymbol{\chi}_{ee} & \boldsymbol{\chi}_{em} \\ \boldsymbol{\chi}_{me} & \boldsymbol{\chi}_{mm} \end{pmatrix} = 2\begin{pmatrix} \frac{\mathbf{I}}{\eta_1} - \frac{\mathbf{S}_{11}}{\eta_1} - \frac{\mathbf{S}_{21}}{\eta_2} & \frac{\mathbf{I}}{\eta_2} - \frac{\mathbf{S}_{12}}{\eta_1} - \frac{\mathbf{S}_{22}}{\eta_2} \\ \mathbf{N} + \mathbf{N}\mathbf{S}_{11} - \mathbf{N}\mathbf{S}_{21} & -\mathbf{N} + \mathbf{N}\mathbf{S}_{12} - \mathbf{N}\mathbf{S}_{22} \end{pmatrix} \times \begin{pmatrix} \mathbf{I} + \mathbf{S}_{11} + \mathbf{S}_{21} & \mathbf{I} + \mathbf{S}_{12} + \mathbf{S}_{22} \\ \frac{\mathbf{N}}{\eta_1} - \frac{\mathbf{N}\mathbf{S}_{11}}{\eta_1} + \frac{\mathbf{N}\mathbf{S}_{21}}{\eta_2} & -\frac{\mathbf{N}}{\eta_2} - \frac{\mathbf{N}\mathbf{S}_{12}}{\eta_1} + \frac{\mathbf{N}\mathbf{S}_{22}}{\eta_2} \end{pmatrix} \tag{S24}$$

where η_1 and η_2 are the wave impedance in regions 1 and 2, respectively, $\mathbf{I} = \begin{pmatrix} 1 & 0 \\ 0 & 1 \end{pmatrix}$ and $\mathbf{N} = \begin{pmatrix} 0 & -1 \\ 1 & 0 \end{pmatrix}$ are the identity matrix and 90° rotation matrix, respectively. Since the lossless metasurface is placed in free space, both η_1 and η_2 are equal to the wave impedance of free space η_0. It must be noted that the *S* parameters in Eq. S24 is under LP basis, and hence, the ideal Jones matrix of the circular birefringent meta-atom $\widehat{U} = \begin{pmatrix} e^{\frac{i\delta}{2}} & 0 \\ 0 & e^{-\frac{i\delta}{2}} \end{pmatrix} e^{i\phi}$ needs to be converted from CP basis to LP basis as follows (*30*):

$$\mathbf{S}_{21} = \widehat{\Lambda}\widehat{U}\widehat{\Lambda}^{-1} = \begin{pmatrix} \cos\frac{\delta}{2} & -\sin\frac{\delta}{2} \\ \sin\frac{\delta}{2} & \cos\frac{\delta}{2} \end{pmatrix} e^{i\phi} \tag{S25}$$

where $\widehat{\Lambda} = \begin{pmatrix} 1 & 1 \\ -i & i \end{pmatrix}$ is the basis transformation matrix. According to reciprocity and conservation of energy, there are $\mathbf{S}_{21} = \mathbf{S}_{12}{}^{\mathrm{T}}$ and $\mathbf{S}_{11} = \mathbf{S}_{22} = \mathbf{0}$. The mathematical from of Eq. S25 is the same as that of the rotation matrix $\begin{pmatrix} \cos\alpha & -\sin\alpha \\ \sin\alpha & \cos\alpha \end{pmatrix}$, indicating that the circular birefringent meta-atom acts as a polarization rotator to induce a counterclockwise rotation of the incident wave's polarization plane by $\delta/2$. For simplicity, replace $\delta/2$ in Eq. S25 by α and substitute all the *S* parameters into Eq. S24, the ideal susceptibilities are obtained:

$$\begin{aligned} \boldsymbol{\chi}_{ee} &= -\frac{i}{\eta_0}\frac{2\sin\phi}{\cos\alpha + \cos\phi}\mathbf{I} = \chi_{ee}\mathbf{I}, \qquad \boldsymbol{\chi}_{em} = \frac{2\sin\alpha}{\cos\alpha + \cos\phi}\mathbf{I} = \chi_{em}\mathbf{I} \\ \boldsymbol{\chi}_{me} &= -\frac{2\sin\alpha}{\cos\alpha + \cos\phi}\mathbf{I} = \chi_{me}\mathbf{I}, \quad \boldsymbol{\chi}_{mm} = -i\eta_0\frac{2\sin\phi}{\cos\alpha + \cos\phi}\mathbf{I} = \chi_{mm}\mathbf{I} \end{aligned} \tag{S26}$$

All the tensors present an identity matrix form, hence, and only 4 of the 16 susceptibilities in Eq. S22 are unique, which are denoted as χ_{ee}, χ_{em}, χ_{me}, and χ_{mm}, respectively. Due to the presence of magnetoelectric coupling and all the susceptibility tensors exhibiting identity matrix form, such medium is classically termed as a bi-isotropic medium (*31*).

Then, the relationship between *S* parameters and the four unique susceptibilities is further analyzed, which can reveal the underlying relationship between constitutive and propagation characteristics. The *S* parameters of the bi-isotropic meta-atom can be calculated reversely from susceptibilities as follows (*29*)

$$\begin{pmatrix} S_{11}^{xx} \\ S_{11}^{yx} \\ S_{21}^{xx} \\ S_{21}^{yx} \end{pmatrix} = C \begin{pmatrix} 2(\chi_{mm} - \eta_0^2 \chi_{ee}) \\ 2\eta_0(\chi_{me} + \chi_{em}) \\ (\chi_{me}\chi_{em} - \chi_{ee}\chi_{mm} + 4) \\ 2\eta_0(\chi_{me} - \chi_{em}) \end{pmatrix} \tag{S27}$$

where $C = \frac{1}{(\eta_0\chi_{ee}+2)(2\eta_0+\chi_{mm})-\eta_0\chi_{me}\chi_{em}}$. According to Eq. S27, the linearly co- and cross-polarized reflection can be completely suppressed by engineering $\eta_0\chi_{ee} = \chi_{mm}/\eta_0$ and $\chi_{em} = -\chi_{me}$. As for the linearly co- and cross-polarized, it is necessary to introduce and tune the magnetoelectric response delicately. When all the tensors are designed to agree with Eq. S26, we can achieve the reflectionless circular birefringent meta-atom perfectly.

Next, we characterize the designed meta-atom by GSTCs theory to demonstrate its excellent circular birefringence. Take meta-atom No. 1 in Fig. S6 (the same as No. 1 in the main text) as example, whose relative rotation angle $\theta = 90°$ and the ideal linearly cross-polarized transmittance reaches unity. Under the y-LP incident wave, the amplitude and phase of transmittance S_{21}^{yy}, S_{21}^{xy} and reflectance S_{11}^{yy}, S_{11}^{xy} are depicted in Fig. S9A and B, where the linearly cross-polarized transmittance S_{21}^{xy} (red solid curve) is the dominant response across the operating bandwidth (8.8 GHz - 14.9 GHz), exhibiting an amplitude above 0.9 and accompanied by a smooth phase variation. Substituting the complex transmittance and reflectance into Eq. S24, the susceptibilities are obtained and shown in Fig. S9C and D, where the solid black curve is the susceptibilities under ideal conditions ($|S_{21}^{xy}| = 1$), providing a clear visual reference for evaluating the deviation of the realized susceptibilities from their ideal values.

Fig. S9C clearly shows that Im($\chi_{ee}\eta_0$) and Im(χ_{mm}/η_{0e}) maintain near-equality across a broad frequency band from 8.8 GHz to 15.9 GHz, which effectively suppresses the linearly co-polarized reflection and thus $|S_{11}^{yy}|$ is below 0.4. Meanwhile, the Re(χ_{em}) and Re(χ_{me}) in Fig. S9D are always opposite, leading to linearly cross-polarized reflectance S_{11}^{xy} almost zero across the broad frequency band. When comparing the realized values with the ideal values (black curves), all the realized values are approximately equal to the ideal value in the operating bandwidth from 8.8 GHz to 14.9 GHz. As a result, both reflection and linearly co-polarized transmission are effectively suppressed in the specified frequency range, enabling the cross-polarized response to become the dominant response.

Through the GSTCs model, we have figured out that the equivalent surface susceptibilities of the designed meta-atom are close to the ideal ones, enabling excellent circular birefringence properties. In addition, we can qualitatively explain the relationship between the structure of meta-atom and resonance. (1) Structure's C_{4z} symmetry (chiral four-fold rotation about the *z*-axis) ensures the isotropic constitutive property, which constrains the tensors in Eq. S22 to exhibit an identity form. (2) The vertical vias establish direct coupling between the connected patches, enabling the introduction of magnetoelectric coupling and results in non-zero values for both $\boldsymbol{\chi}_{em}$ and $\boldsymbol{\chi}_{me}$. (3) The metal ground plane not only effectively isolates the receiving and transmitting layers to enhance the robustness of the manipulation, but also supports current that is opposite to the patches to strengthen resonance, and consequently broaden the transmission bandwidth and improve the efficiency.

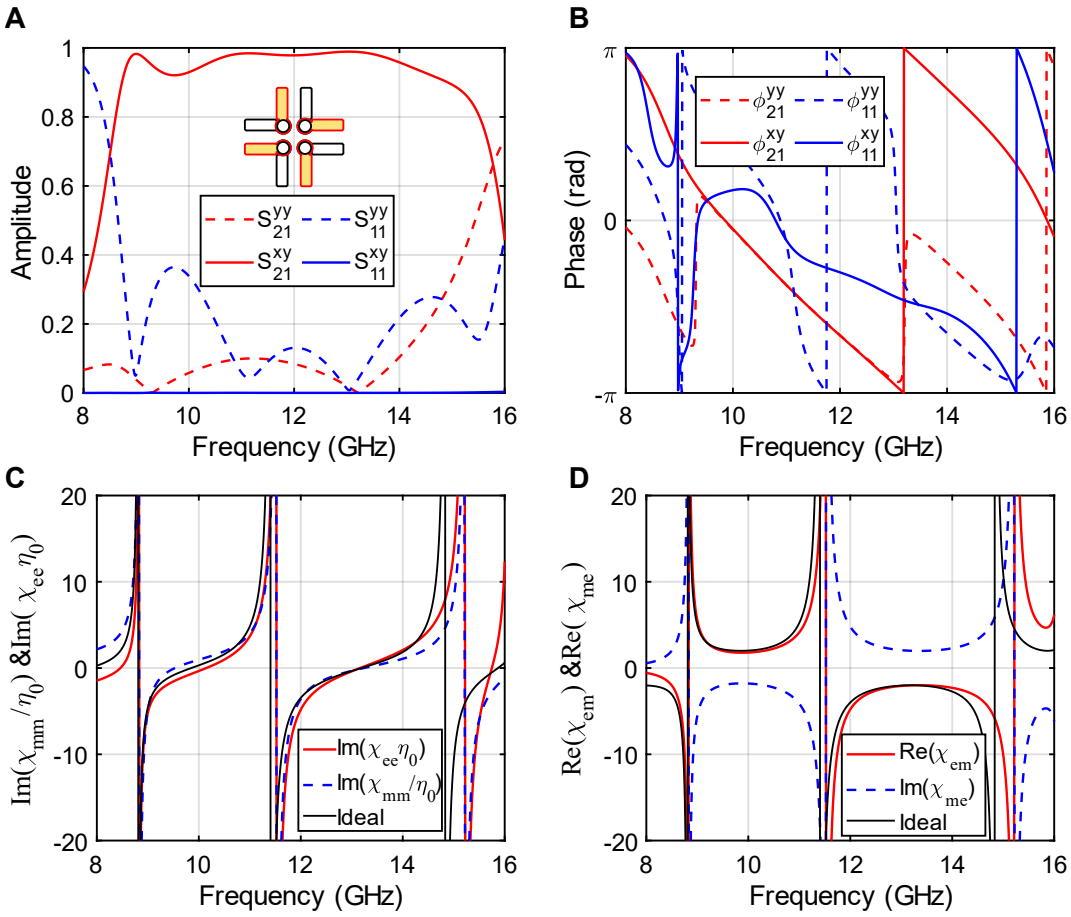

Fig. S9. The *S* parameter and the Susceptibilities of the demonstration meta-atom. (**A**) The amplitude and (**B**) phase of transmittance S_{21}^{yy} (red dashed curve), S_{21}^{xy} (red solid curve) and reflectance S_{11}^{yy} (blue dashed curve), S_{11}^{xy} (blue solid curve). The (**C**) imaginary part of $\chi_{ee}\eta_0$ (red solid curve) and χ_{mm}/η_0 (blue dashed curve), (**D**) real part of χ_{em} (red solid curve) and χ_{em} (blue dashed curve), and the black solid curves are the ideal result when $S_{11}^{xy} = 1$.

Supplementary Note 5: Fabrication of metasurface prototypes, measurement methods and transmission efficiency characterization

Fabrication of metasurface prototypes

All the proposed metasurface prototypes are fabricated by printed circuit board (PCB) technology and consist of two 2.5 mm thick FB430 dielectric substrates. The copper films on each substrate are etched into the design patterns and then a 0.1 mm thick bonding layer is used to stick the dielectric substrates tightly. To form the vertical metal vias, holes are drilled in the PCBs and a thin layer of copper coating is deposited chemically on the inner wall of the holes.

Measurement methods

The experimental setup is schematically depicted in Fig. S10A. The receiving and transmitting antennas are both linearly polarized. To obtain the results under circular polarization states, both the co- and cross-polarized transmission fields under *x*- and *y*-LP incident waves are measured. Then the transmitted electric field for any polarization state can be obtained according to the polarization synthesis.

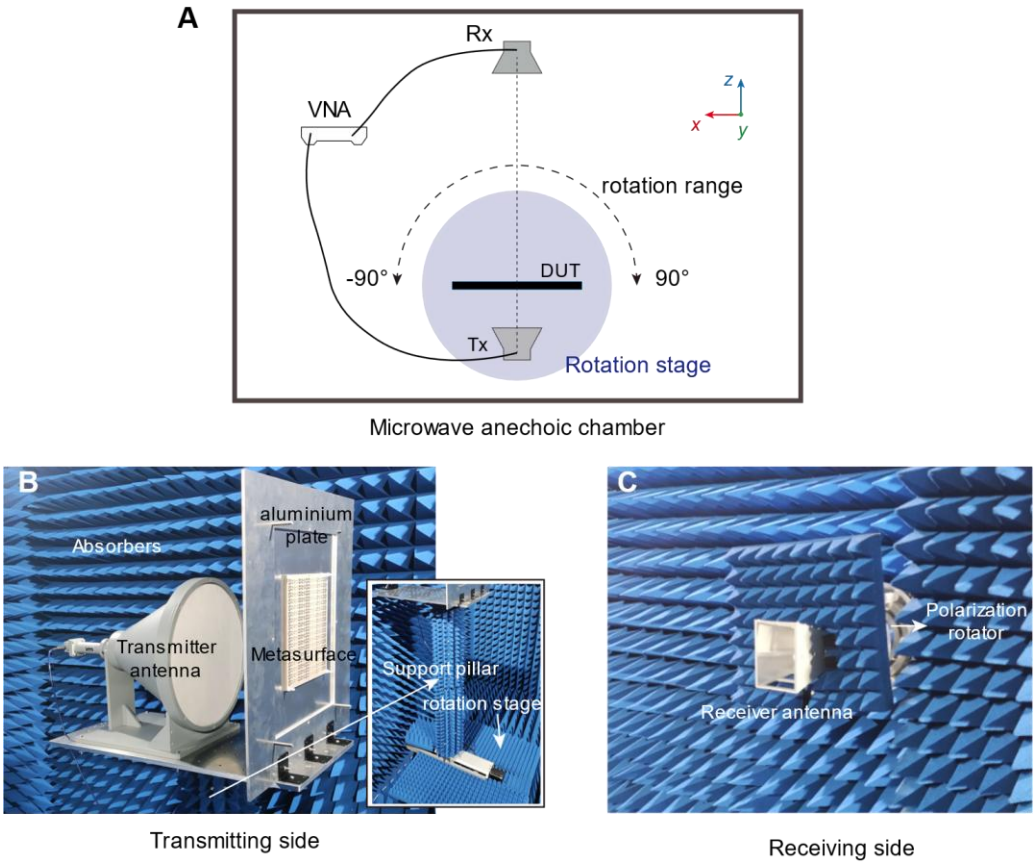

Fig. S10. Experimental setup for metasurface measurement. (A) The measurements are conducted in a microwave anechoic chamber, where the metasurface, transmitting (Tx) antenna and receiving (Rx) antenna are horizontally and vertically aligned. The antennas are connected to a Keysight P9384B vector network analyzer (VNA) to extract the scattering parameters. (B) On the transmission side, a rotation stage supporting a turn table to hold the metasurface and transmitter antenna is used. The metasurface under test is placed at the rotation center of the stage and the dielectric lens-loaded high gain horn antenna placed 200 mm in front of the metasurface

is used as the illumination source. On the receiving side, a dual-ridged horn antenna placed 2.5 m (83λ at 10 GHz) away from the metasurface is used to collect the transmitted intensities.

Transmission efficiency characterization

Based on the measured far-field results of the two metasurface prototypes, their transmission efficiencies are calculated to characterize the high efficiency merit:

$$T_{ij} = \frac{\sum_{-90^\circ}^{90^\circ} \left|E_{ij}(\theta)\right|^2}{\sum_{-90^\circ}^{90^\circ} |E_0(\theta)|^2} \tag{S28}$$

where subscripts i, j can be + or − representing the RHCP and LHCP respectively, $E_{ij}(\theta)$ is the amplitude of the measured electric field scattered from metasurface at an angle θ, while $E_0(\theta)$ is the far-field pattern of the transmitting antenna without metasurface, which act as the reference for the efficiency evaluation.

The transmission efficiency within 8 GHz - 12 GHz of the antisymmetric refractor in Fig. 4A is shown in Fig. S11, where co-polarized transmission efficiency T_{++} and T_{--} are pretty similar and mostly over 0.6 within 8.2 GHz -11.7 GHz, where the maximum is around 0.93 at 10.9 GHz, but drop a bit within 9.2 GHz - 9.6 GHz. Meanwhile, cross-polarized transmission efficiency T_{+-} and T_{-+} remain predominantly below 0.1, indicating that cross-polarized transmission is effectively suppressed and thus demonstrating the dominance of co-polarized transmission. As for the asymmetric refractor in Fig. 4D, its T_{++} and T_{--} are slightly different within 8 GHz - 9.5 GHz and mostly over 0.6 within 8.5 GHz - 12 GHz, and the maximum is around 0.88 at 10.8 GHz, as presented in Fig. S12. These results confirm that co-polarized transmission remains the dominant response. Apparently, the experimental results demonstrate that both metasurfaces maintain high co-polarized transmission efficiency from 8 GHz to 12 GHz, thereby validating the superior performance of the proposed metasurface designs.

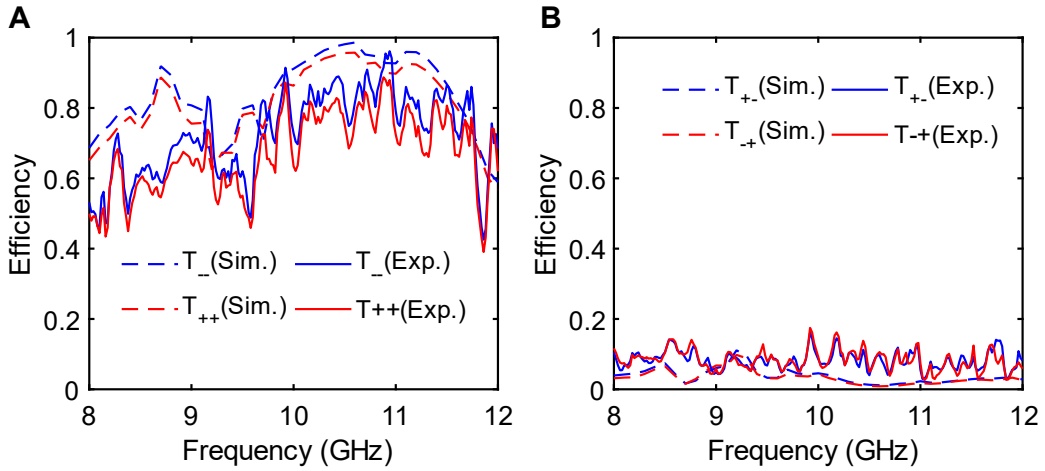

Fig. S11. The transmission efficiency of antisymmetric refractor (corresponding to metasurface in Fig. 4A in the main text). The experimental (solid) and measured (dashed) transmission efficiency of (A) co- and (B) cross-polarized channels under RHCP (red) and LHCP (blue) incident wave.

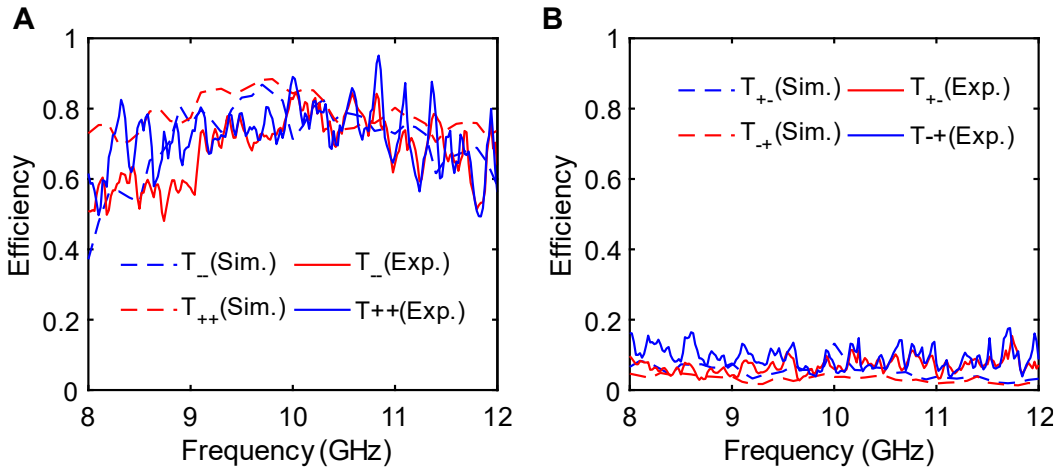

Fig. S12. The transmission efficiency of asymmetric refractor (corresponding to metasurface in Fig. 4D in the main text). The experimental (solid) and measured (dashed) transmission efficiency of (A) co- and (B) cross-polarized channels under RHCP (red) and (LHCP) incident wave.

Despite certain fluctuations in the experimental results, there is still a good agreement with the simulation results. The discrepancies between simulations and experiments can be attributed to many factors such as fabrication errors of the prototype, imperfect uniformity of the horn antenna's radiation pattern, phase instability in the vector network analyzer during measurement, and alignment inaccuracies of the devices.

Supplementary Note 6: Decoupling of two-dimensional wavefront

Besides the asymmetric refraction metasurface with decoupled one-dimension phase profile in the main text, here, a metasurface with decoupled two-dimensional phase profile is proposed and further demonstrated. The target functionalities are focusing and vortex wave generation for RHCP and LHCP incident waves, respectively, and their phase profiles (Φ_{++} and Φ_{--}), presented in Fig. S13A are

$$\Phi_{++} = \frac{2\pi f_c}{c}\left(\sqrt{x^2 + y^2 + F^2} - F\right) \tag{S29}$$

$$\Phi_{--} = l \cdot \mathrm{atan2}(y, x) \tag{S30}$$

where x and y are the central coordinates of each meta-atom, F is the focal length for focusing, and l is the topological charge of orbital angular momentum (OAM) of the vortex wave. Here, f_c = 10 GHz, F = 150 mm and l = 1, and the design of the metasurface is shown in Fig. S13B.

Fig. S13C and E show the normalized co- and cross-polarized near-field E_{++} and E_{-+} under RHCP illumination, E_{++} presents a clear focusing property on the *yoz* plane, where the focal center is around z = 100 mm and the field in the corresponding *xoy* plane show a clear focusing spot. As for E_{-+}, the intensity is much darker, proving that cross-polarized transmission is almost absent and thus co-polarized transmission is dominant. Similarly, under LHCP illumination (Figs. S13D and F), E_{--} is a split beam in the *yoz* plane and presents a hollow ring on the *xoy* plane, showing a clear vortex beam property, and we can see a counterclockwise spiral phase from the phase distribution in the inset, proving the topological charge of OAM is 1. The above results prove that the metasurface performs distinct 2D functionalities in the two orthogonal co-polarized transmission channels, further validating the proposed strategy for wavefront decoupling.

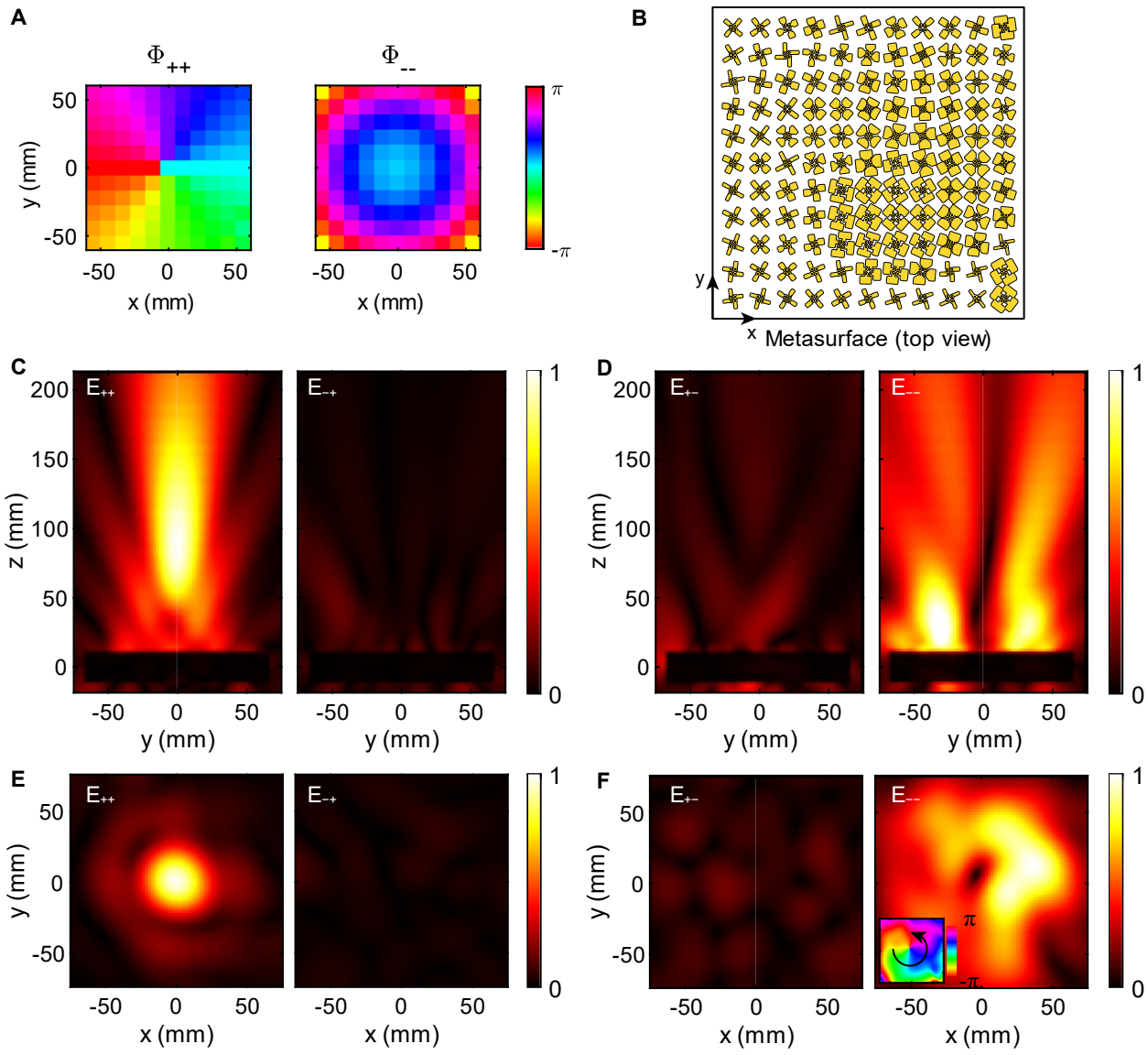

Fig. S13. Result of the two-dimensional decoupled metasurface. (A) The phase profile $\Phi_{++}(x, y)$ and $\Phi_{--}(x, y)$ of the decoupled metasurface. (**B**) The top view of the metasurface. (**C** and **D**) The normalized near-field of the co- and cross-polarized components on the *yoz* plane under the illumination of RHCP and LHCP wave (10 GHz). (**E** and **F**) The normalized near-field of the co- and cross-polarized components on the *xoy* plane at z = 100 *mm*, and the inset is the phase of E_{--}.

Supplementary Note 7: Singularity under generic polarization state

The polarization basis of the Jones matrix in Eq. S3 is determined by the polarization at the poles of the sphere, which are orthogonal CP states. Therefore, if the polarization at the poles is replaced by a pair of orthonormal bases $|\psi_+\rangle$ and $|\psi_-\rangle$, the co-polarized channels are under this polarization basis and can be analyzed in the same way. The new Poincaré sphere whose poles are $|\psi_+\rangle$ and $|\psi_-\rangle$ can be obtained by rotating the original sphere around the origin. For simplicity, the cartesian coordinate of original and new spheres is denoted as $\mathbf{S} = (S_1, S_2, S_3)^{\mathrm{T}}$ and $\mathbf{S}' = (S_1', S_2', S_3')^{\mathrm{T}}$, respectively, their relationship is

$$\mathbf{S}' = \mathbf{R} \times \mathbf{S} \tag{S31}$$

and the matrix **R** is the three-dimensional rotation matrix follows

$$\mathbf{R} = \begin{pmatrix} \hat{u}_x' \\ \hat{u}_y' \\ \hat{u}_z' \end{pmatrix} = \begin{pmatrix} u_{x,x}' & u_{y,x}' & u_{z,x}' \\ u_{x,y}' & u_{y,y}' & u_{z,y}' \\ u_{x,z}' & u_{y,z}' & u_{z,z}' \end{pmatrix} \tag{S32}$$

$\hat{u}_x' = \left(u_{x,x}', u_{y,x}', u_{z,x}'\right)$, $\hat{u}_x'$ is the unit *x*-vector on coordinate **S**' and it is projected to the original coordinate **S**. $u_{x,x}'$, $u_{y,x}'$, $u_{y,x}'$ are the projection components of u_x' on the original *x*-, *y*- and *z*-axis, where the first subscript denotes the projection component of coordinate **S**, and the second subscript denotes the component of coordinate **S**'.

To obtain the matrix **R**, it is necessary to calculate $\hat{u}_x', \hat{u}_y', \hat{u}_z'$. First, the state of the new *z*-axis (S_3-axis) is $|\psi_+\rangle$, the unit vector $\hat{u}_z'$ is its Stokes vector. Second, the state of the new *x*-axis (S_1-axis) is $\frac{\sqrt{2}}{2}|\psi_+\rangle + \frac{\sqrt{2}}{2}|\psi_-\rangle$ and its Stokes vector is $\hat{u}_x'$. Third, the new *y*-axis (S_2-axis) can be obtained by the cross-product of u_z' and u_x', i.e. $u_y' = u_z' \times u_x'$. Here are their analytical math expressions

$$\hat{u}_x' = \begin{pmatrix} -\sin 2\psi \\ \cos 2\psi \\ 0 \end{pmatrix}, \hat{u}_y' = \begin{pmatrix} -\sin 2\chi \cos 2\psi \\ -\sin 2\chi \sin 2\psi \\ \cos 2\chi \end{pmatrix}, \hat{u}_z' = \begin{pmatrix} \cos 2\chi \cos 2\psi \\ \cos 2\chi \sin 2\psi \\ \sin 2\chi \end{pmatrix} \tag{S33}$$

where χ and ψ are the parameters of original sphere, and the rotation matrix **R** is

$$\mathbf{R} = \begin{pmatrix} -\sin 2\psi & \cos 2\psi & 0 \\ -\sin 2\chi \cos 2\psi & -\sin 2\chi \sin 2\psi & \cos 2\chi \\ \cos 2\chi \cos 2\psi & \cos 2\chi \sin 2\psi & \sin 2\chi \end{pmatrix} \tag{S34}$$

Thus, the transformation relation between **S** and **S**' is

$$\mathbf{S}' = \mathbf{R} \times \mathbf{S} = \begin{pmatrix} S_2 \cos 2\psi - S_1 \sin 2\psi \\ S_3 \cos 2\chi - \sin 2\chi \left(S_1 \cos 2\psi + S_2 \sin 2\psi\right) \\ \cos 2\chi \left(S_1 \cos 2\psi + S_2 \sin 2\psi\right) + S_3 \sin 2\chi \end{pmatrix} = \begin{pmatrix} \cos 2\chi' \cos 2\psi' \\ \cos 2\chi' \sin 2\psi' \\ \sin 2\chi' \end{pmatrix} \tag{S35}$$

where ψ' and χ' are the new azimuth angle and ellipticity, respectively. Then the singularity is shown on the surface of the Poincaré sphere in **S** and **S**' coordinates, respectively, for comparison. The singularity in the original sphere (Fig. S14A), the original and new axes are shown parallel, and the singularity is at the antipole of the S_3' axis. By rotating the new axes and sphere simultaneously, as shown in Fig. S14B, the new sphere is similar to the original one, and it can be expanded in the same way (Fig. S14C). Besides, the Jones matrix under orthonormal bases $|\psi_+\rangle$ and $|\psi_-\rangle$ is denoted as $\hat{U}'$ and can be expressed by coordinate **S**' as

$$\hat{U}' = \exp\left(i\frac{\delta}{2}\mathbf{S}' \cdot \hat{\boldsymbol{\sigma}}^* + i\phi\right) \tag{36}$$

The form is the same as Eq. 1 in the main text, but the polarization base is different. Therefore, the singularity of arbitrary co-polarized channel can be found on the surface of the Poincaré sphere in the same way, proving the generality of the proposed phase mechanism.

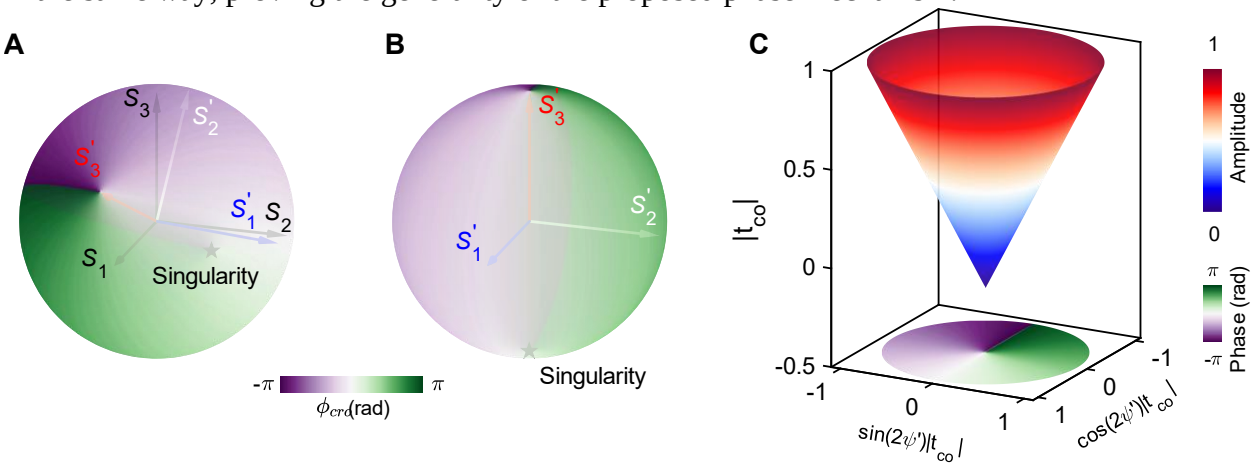

Fig. S14 The singularity on the surface sphere under arbitrary polarized co-channel. (A) The singularity and phase on the sphere under arbitrary polarization $|\boldsymbol{\psi}_+\rangle$. Stokes vector of $|\boldsymbol{\psi}_+\rangle$ is the $\boldsymbol{S_3'}$ axis and its antipole is the singularity. (B) Rotate the sphere and the new axis to align with the original axis orientation, the singularity is at the new south pole. (C) Expansion of the rotated sphere.

References and Notes

1. S. Pancharatnam, Generalized theory of interference, and its applications. Proc. Indian Acad. Sci. A. 44, 247-262 (1956).
2. Berry M V 1984 Quantal phase factors accompanying adiabatic changes *Proc. R. Soc.* A 392 45–57.
3. Aharonov, Y. & Bohm D. Significance of electromagnetic potentials in the quantum theory. Phys. Rev. 11, 485 (1959).
4. Samuel, Joseph, and Rajendra Bhandari. "General setting for Berry's phase." *Physical Review Letters* 60.23 (1988): 2339.
5. Shapere, Alfred, and Frank Wilczek, eds. *Geometric phases in physics*. Vol. 5. World scientific, 1989.
6. Zak, J. "Berry's phase for energy bands in solids." *Physical review letters* 62.23 (1989): 2747.
7. Dattoli, G., R. Mignani, and A. Torre. "Geometrical phase in the cyclic evolution of non-Hermitian systems." *Journal of Physics A: Mathematical and General* 23.24 (1990): 5795.
8. Cayssol, Jérôme, and Jean-Noël Fuchs. "Topological and geometrical aspects of band theory." *Journal of Physics: Materials* 4.3 (2021): 034007.
9. Bliokh, Konstantin Yu, et al. "Spin–orbit interactions of light." *Nature Photonics* 9.12 (2015): 796-808.
10. Cohen, Eliahu, et al. "Geometric phase from Aharonov–Bohm to Pancharatnam–Berry and beyond." *Nature Reviews Physics* 1.7 (2019): 437-449.
11. Ferrer-Garcia, Manuel F., et al. "Topological transitions of the generalized Pancharatnam-Berry phase." *Science advances* 9.47 (2023).
12. Dennis, Mark R., Kevin O'holleran, and Miles J. Padgett. "Singular optics: optical vortices and polarization singularities." *Progress in optics*. Vol. 53. Elsevier, 2009. 293-363.
13. Bauer, Thomas, et al. "Observation of optical polarization Möbius strips." *Science* 347.6225 (2015): 964-966.
14. Bliokh, Konstantin Y., Miguel A. Alonso, and Mark R. Dennis. "Geometric phases in 2D and 3D polarized fields: geometrical, dynamical, and topological aspects." *Reports on Progress in Physics* 82.12 (2019): 122401.
15. Jisha, Chandroth Pannian, Stefan Nolte, and Alessandro Alberucci. "Geometric phase in optics: from wavefront manipulation to waveguiding." *Laser & Photonics Reviews* 15.10 (2021): 2100003.
16. Yin, Xiaobo, et al. "Photonic spin Hall effect at metasurfaces." *Science* 339.6126 (2013): 1405-1407.
17. Slussarenko, Sergei, et al. "Guiding light via geometric phases." *Nature Photonics* 10.9 (2016): 571-575.
18. Balthasar Mueller, J. P., et al. "Metasurface polarization optics: independent phase control of arbitrary orthogonal states of polarization." *Physical review letters* 118.11 (2017): 113901.
19. Devlin, Robert C., et al. "Arbitrary spin-to–orbital angular momentum conversion of light." *Science* 358.6365 (2017): 896-901.
20. Maguid, Elhanan, et al. "Multifunctional interleaved geometric-phase dielectric metasurfaces." *Light: Science & Applications* 6.8 (2017): e17027-e17027.
21. Song, Qinghua, et al. "Ptychography retrieval of fully polarized holograms from geometric-phase metasurfaces." *Nature communications* 11.1 (2020): 2651.
22. Song, Qinghua, et al. "Plasmonic topological metasurface by encircling an exceptional point." *Science* 373.6559 (2021): 1133-1137.

23. Choudhury, Sajid, et al. "Pancharatnam–Berry phase manipulating metasurface for visible color hologram based on low loss silver thin film." *Advanced Optical Materials* 5.10 (2017): 1700196.
24. Ding, Xumin, et al. "Ultrathin Pancharatnam–Berry metasurface with maximal cross-polarization efficiency." *Advanced materials* 27.7 (2015): 1195-1200.
25. Luo, Weijie, et al. "Photonic spin Hall effect with nearly 100% efficiency." *Advanced Optical Materials* 3.8 (2015): 1102-1108.
26. Song, Q., et al. "Bandwidth-unlimited polarization-maintaining metasurfaces." *Science advances* 7.5 (2021): eabe1112.
27. Engay, Einstom, et al. "Transverse optical gradient force in untethered rotating metaspinners." *Light: Science & Applications* 14.1 (2025): 38.
28. Holloway, Christopher L., et al. "An overview of the theory and applications of metasurfaces: The two-dimensional equivalents of metamaterials." *IEEE antennas and propagation magazine* 54.2 (2012): 10-35.
29. Pfeiffer, Carl, and Anthony Grbic. "Bianisotropic metasurfaces for optimal polarization control: Analysis and synthesis." *Physical Review Applied* 2.4 (2014): 044011.
30. Menzel, Christoph, Carsten Rockstuhl, and Falk Lederer. "Advanced Jones calculus for the classification of periodic metamaterials." *Physical Review A—Atomic, Molecular, and Optical Physics* 82.5 (2010): 053811.
31. Caloz, Christophe, and Ari Sihvola. "Electromagnetic chirality, part 1: the microscopic perspective [electromagnetic perspectives]." *IEEE Antennas and Propagation Magazine* 62.1 (2020): 58-71.